

# “Ship in a Bottle” Design of Highly Efficient Bifunctional Electrocatalysts for Long-Lasting Rechargeable Zn–Air Batteries

Zhen Zhang,<sup>†</sup> Ya-Ping Deng,<sup>†</sup> Zhenyu Xing,<sup>†,‡</sup> Dan Luo,<sup>†</sup> Serubbabel Sy,<sup>†</sup> Zachary Paul Cano,<sup>†</sup> Guihua Liu,<sup>†</sup> Yi Jiang,<sup>†</sup> and Zhongwei Chen<sup>\*,†</sup>

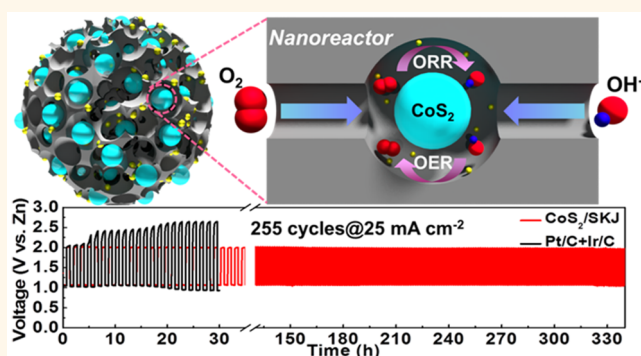
<sup>†</sup>Department of Chemical Engineering, Waterloo Institute for Nanotechnology, Waterloo Institute for Sustainable Energy, University of Waterloo, Waterloo, Ontario N2L 3G1, Canada

<sup>‡</sup>School of Chemistry and Environment, South China Normal University, Guangzhou 510006, China

## Supporting Information

**ABSTRACT:** The poor durability of bifunctional oxygen electrocatalysts is one main bottleneck that suppresses the widespread application of rechargeable metal–air batteries. Herein, a “ship in a bottle” design is achieved by impregnating fine transition metal dichalcogenide nanoparticles into defective carbon pores that act as interconnected nanoreactors. The erected 3D porous conductive architecture provides a “highway” for expediting charge and mass transfer. This design not only delivers a high surface-to-volume ratio to increase numbers of exposed catalytic sites but also precludes nanoparticles from aggregation during cycling owing to the pore spatial confinement effect. Therefore, the long-term plague inherent to nanocatalyst stability can be solved. Moreover, the synergistic coupling effects between defect-rich interfaces and chemical bonding derived from heteroatom-doping boost the catalytic activity and prohibit the detachment of nanoparticles for better stability. Consequently, the developed catalyst presents superior bifunctional oxygen electrocatalytic activities and durability, out-performing the best-known noble-metal benchmarks. In a practical application to rechargeable Zn–air batteries, long-term cyclability for over 340 h is realized at a high current density of 25 mA cm<sup>-2</sup> in ambient air while retaining an intact structure. Such a universal “ship in a bottle” design offers an appealing and instructive model of nanomaterial engineering for implementation in various fields.

**KEYWORDS:** bifunctional catalysts, oxygen electrocatalysis, nanostructure design, defective carbon, Zn–air batteries, long-term cyclability



The recognition of global overconsumption of fossil fuels and associated environmental deterioration has spurred a strong imperative for the development of next-generation sustainable energy storage and conversion systems.<sup>1,2</sup> The urgency is to develop inexpensive renewable energy storage technologies with high energy densities to reduce dependence on conventional fossil fuels. Rechargeable metal–air batteries are attracting renewed interest as a promising energy storage system because of the high energy density and enhanced safety as well as environmental compatibility.<sup>3</sup> In particular, a Zn–air battery can theoretically store energy of as much as 1086 Wh kg<sup>-1</sup>, up to 4 times higher than currently widely used lithium-ion batteries. The attractive energy density is derived from an open-cell configuration wherein a zinc anode is coupled with an air-breathing cathode that uses oxygen in atmospheric air as fuel for the

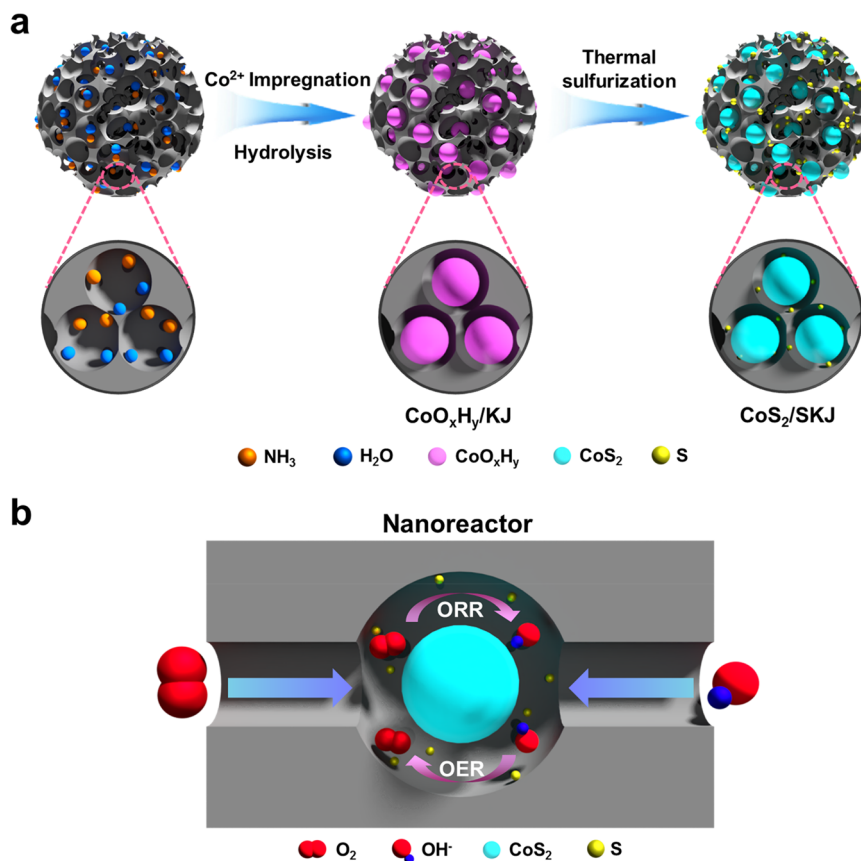
electrochemical reactions.<sup>4,5</sup> However, their widespread practical applications are largely hindered by the unsatisfactory rechargeability (*i.e.*, lifetime) and low energy conversion efficiency, which mainly stem from the challenges encountered at the air cathode with sluggish kinetics and poor electrochemical stability for the repeated oxygen reduction (ORR) and evolution (OER) reactions.<sup>6,7</sup> Therefore, the development of efficient and durable bifunctional electrocatalysts for both ORR and OER plays a pivotal role. Up to now, noble-metal electrocatalysts, such as platinum (Pt) and iridium (Ir), have been intensively investigated and recognized as the most highly active electrocatalysts for ORR or OER.<sup>8</sup> Unfortunately, their

Received: March 25, 2019

Accepted: May 16, 2019

Published: May 16, 2019

Scheme 1. Schematic Illustration of (a) the Synthesis Route of CoS<sub>2</sub>/SKJ and (b) the Individual Pore Acting as the Nanoreactor for Oxygen Electrocatalysis



high cost, unsatisfactory catalytic bifunctionality, and stability inevitably preclude their widespread applications.<sup>9,10</sup>

Non-precious-metal based materials hybridized with carbon have become promising candidates for high-performance Zn–air batteries.<sup>11,12</sup> Recently, numerous synthesis strategies have been reported, mainly including metal deposition onto carbon-based supports or carbon coating on metal particles.<sup>13–16</sup> However, the former method cannot efficiently immobilize metal nanoparticles and control their growth during synthesis and even catalytic reactions, which may cause the loss or aggregation of nanoparticles and thus degrade their electrocatalytic durability and performance. Although the latter method can form a carbon-sealed confined space for metal-based particles, the absence of high and uniform porosity for sufficient mass transfer, as well as inefficient control of nanoparticle size and structural change due to poor consistency of the carbon-coating thickness, lead to limited electrocatalytic performance. Furthermore, numerous advantages of the carbon support should be exploited beyond its role as a nanomaterial carrier, which potentially include defect-induced modification and synergistic effects for enhanced electrocatalytic performance.<sup>17,18</sup> Therefore, a rational structural design combined with defect engineering is critical to achieve a high bifunctional catalytic activity with enhanced durability.

Herein, we report a “ship in a bottle” nanocatalyst design based on fine pyrite-phase transition metal dichalcogenide nanoparticles rooted inside defective carbon pores. The pores function as individual nanoreactors that are interconnected with one another, in which oxygen catalysis efficiently proceeds under the steric pore environment. As a proof-of-concept,

cobalt pyrite (CoS<sub>2</sub>) was selected as a model material because of its abundance and intrinsically conductive metallic nature.<sup>19</sup> This design delivers multiple advantages: (i) the nucleation of CoS<sub>2</sub> nanoparticles is controlled due to the spatial confinement effect of the carbon pores, which not only restricts nanoparticle overgrowth to guarantee a high surface-to-volume ratio and increase numbers of exposed catalytic sites but also prevents nanoparticles from aggregating during catalysis, solving the long-term issue of nanocatalyst stability; (ii) the interpenetrating and interconnecting porous carbon framework builds up a 3D conductive architecture as the nanoreactor to provide a “highway” for electron and mass transfer and facilitate fast catalytic kinetics; and (iii) the synergistic coupling effects between defect-rich interfaces and chemical bonding derived from sulfur doping boost the catalytic activity and prohibit the detachment of nanoparticles. The resultant catalyst presents a superior bifunctional electrocatalytic activity and durability toward ORR and OER and demonstrates excellent performance and long-term cyclability in the rechargeable Zn–air battery.

## RESULTS AND DISCUSSION

A facile and universal impregnation strategy to achieve the recessed growth of CoS<sub>2</sub> nanoparticles inside heteroatom-doped, defective carbon pores is illustrated in Scheme 1a. Ketjen Black EC600JD (KJ) carbon with adsorbed water vapor and ammonia functions as a porous built-in reaction host, whose microscopic morphology is shown in Figure S1a–c. After KJ carbon was soaked in cobalt(II) acetylacetonate organic solution, the cobalt precursor is hydrolyzed inside the

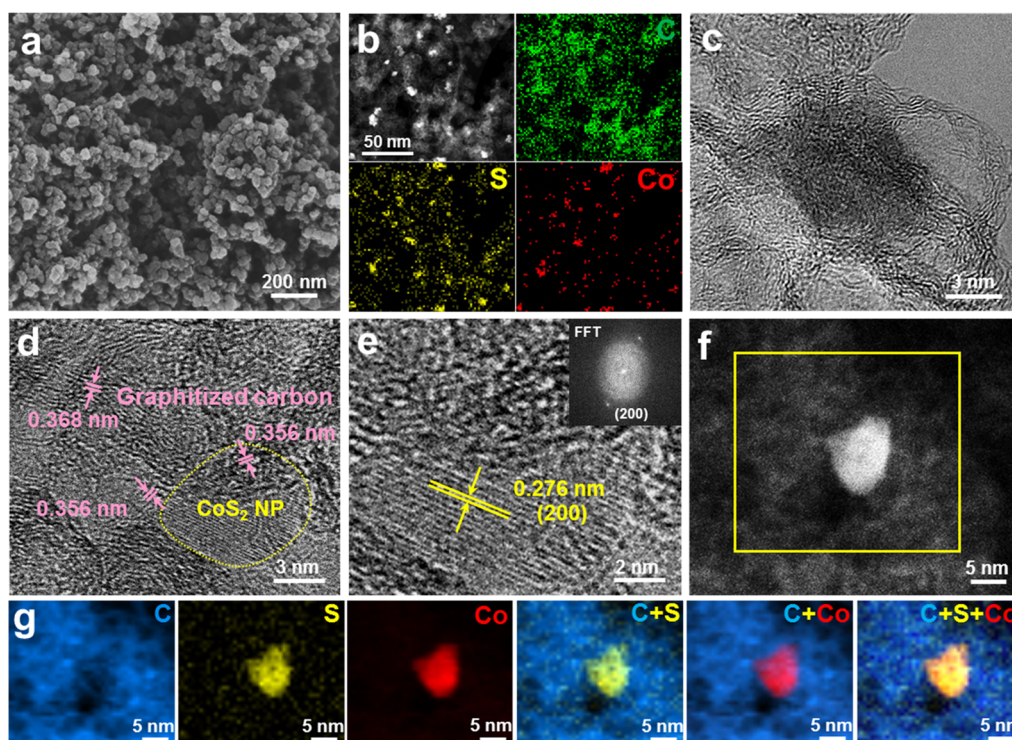


**Figure 1.** (a) Overview SEM and (b) STEM images of CoS<sub>2</sub>/SKJ as well as corresponding EDS mapping images. (c) TEM image of CoS<sub>2</sub>/SKJ. (d) HRTEM image of graphitized carbon intimately surrounding CoS<sub>2</sub> nanoparticles. (e) HRTEM image and corresponding FFT diffraction pattern. (f) STEM image and (g) corresponding EELS elemental mapping and overlaid images of a single CoS<sub>2</sub> nanoparticle immobilized inside carbon pores.

carbon pores under the alkaline environment derived from absorbed ammonia. Following this, the cobalt-hydrolyzed product undergoes thermal sulfurization, yielding the final product, in which CoS<sub>2</sub> is immobilized inside the S-doped, defective carbon pores (CoS<sub>2</sub>/SKJ). Each individual pore acts as a nanoreactor, interconnecting with each other for efficient oxygen electrocatalysis, as illustrated in Scheme 1b.

Scanning electron microscopy (SEM) imaging (Figure 1a) reveals a uniform distribution and clean external surface for CoS<sub>2</sub>/SKJ. No obvious morphology change is observed compared to KJ (Figure S1a), and no agglomeration forms on the external carbon surface, implying successful encapsulation of CoS<sub>2</sub> inside the carbon pores. As shown by the scanning transmission electron microscopy (STEM) imaging (Figure 1b), the bright nanodomains are the CoS<sub>2</sub> phase, whereas the dark domains are mainly the C phase from KJ carbon. The corresponding energy-dispersive X-ray spectroscopy (EDS) mapping confirms the presence of Co, S, and C elements in CoS<sub>2</sub>/SKJ, and the homogeneous distribution of Co and S demonstrates that abundant CoS<sub>2</sub> active sites were exposed and dispersed uniformly throughout the porous carbon host. As shown in Figure 1c, the high-resolution transmission electron microscopy (HRTEM) image provides explicit evidence that CoS<sub>2</sub> nanoparticles with a particle size of ~8.0 nm are embedded in the carbon pores. Importantly, such small nanoparticles were maintained after a heat treatment at 450 °C because of the carbon pore confinement effect, which deters the CoS<sub>2</sub> nanoparticles from agglomerating even at high temperatures. The HRTEM image in Figure 1d reveals that the carbon framework intimately contacted with CoS<sub>2</sub> nanoparticles is highly graphitized, and the graphitization occurs not only around the CoS<sub>2</sub>-loaded pores but also throughout the

entire composite, building up an interconnected conductive network to offer fast electron transfer. KJ carbon exhibits a typical C (002) facet with a *d*-spacing around 0.337 nm (Figure S1d), while the graphitized carbon in CoS<sub>2</sub>/SKJ presents slightly larger *d*-spacing (Figure 1d), which is attributed to the successful S-doping within the graphitized carbon skeleton.<sup>20</sup> It is also noteworthy that the massive porous structures interpenetrate and interconnect with each other, creating a 3D nanoreactor architecture for ion transfer inside and through CoS<sub>2</sub>/SKJ, which potentially provides significantly improved kinetics for electrocatalytic processes. The encapsulated CoS<sub>2</sub> demonstrates a high crystallinity of the primary particles, in which the lattice fringes with an interplanar distance of 0.276 nm correspond to the (200) crystal plane of CoS<sub>2</sub>, which is evidenced by the fast Fourier transform (FFT) pattern (Figure 1e).<sup>21,22</sup> The STEM image in Figure 1f shows one isolated CoS<sub>2</sub> nanoparticle with a diameter of around 8.0 nm immobilized within carbon pores, confirming the pore confinement effect, which is also reflected in the nanoparticle size distribution (Figure S2). As revealed in the corresponding electron energy loss spectroscopy (EELS) mapping (Figure 1g), the S element shows a homogeneous dispersion over the carbon skeleton in addition to the central CoS<sub>2</sub> phase, indicating the successful S-doping. The central-domain distribution of Co suggests the sole existence of intact cubic CoS<sub>2</sub>. These results validate the encapsulation of immobilized CoS<sub>2</sub> into the interior pores of the S-doped carbon host. The morphology of commercial CoS<sub>2</sub> is shown in Figure S3. For comparison, a control composite was prepared by mechanically mixing KJ with commercial CoS<sub>2</sub> followed by the same thermal sulfurization process (denoted as CoS<sub>2</sub> plus SKJ). Without the pore confinement effect, CoS<sub>2</sub> plus SKJ

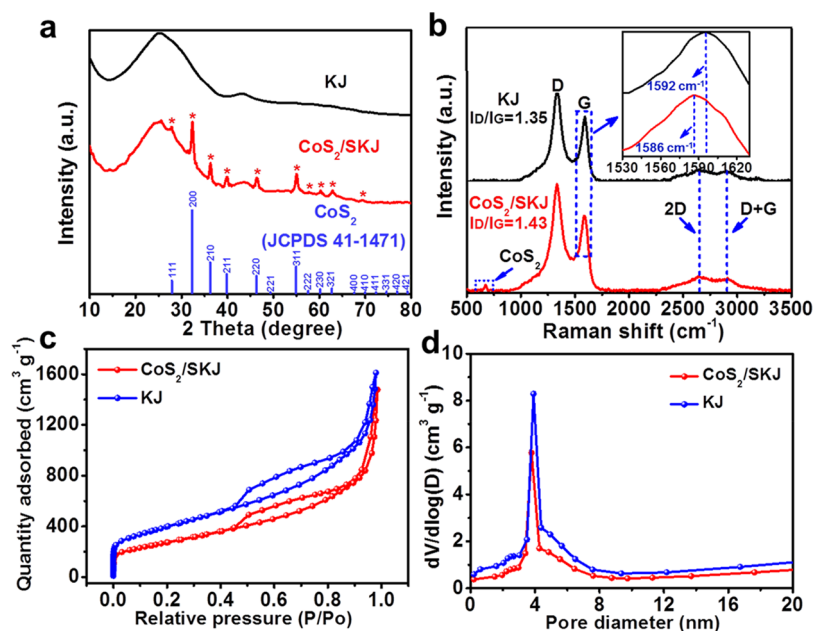


Figure 2. (a) XRD patterns, (b) Raman spectra with a magnified inset, (c)  $N_2$  adsorption–desorption isotherms, and (d) pore size distribution of KJ and  $CoS_2/SKJ$ .

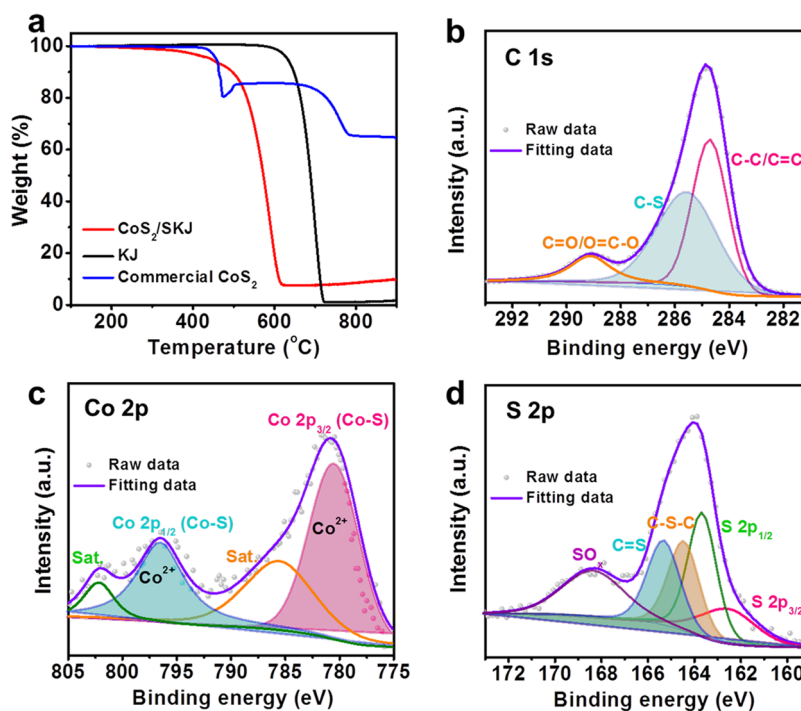
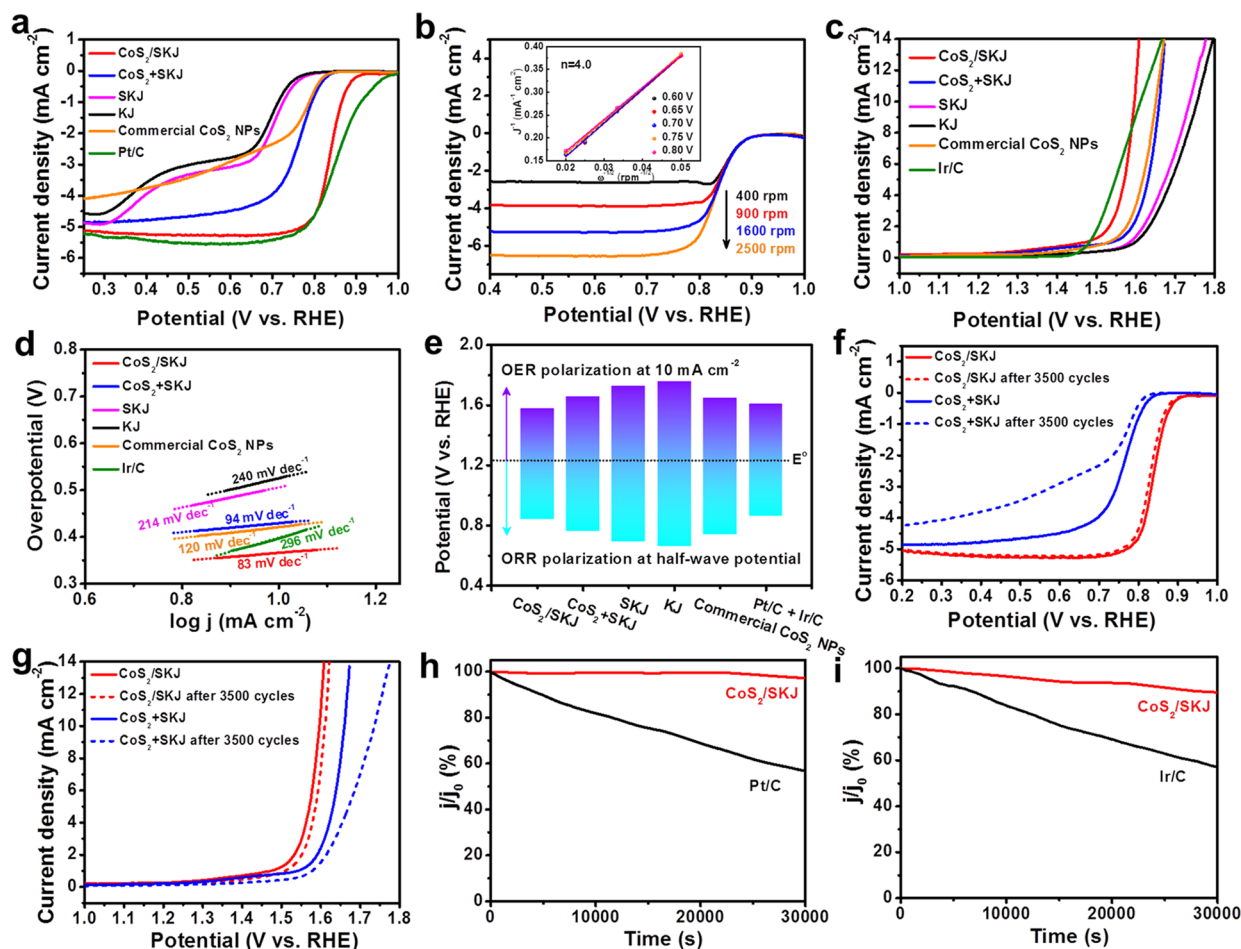


Figure 3. (a) TGA curves of  $CoS_2/SKJ$ , KJ, and commercial pure  $CoS_2$  measured in air; high-resolution XPS spectra of (b) C 1s, (c) Co 2p, and (d) S 2p for  $CoS_2/SKJ$ .

displays much larger  $CoS_2$  particles with a diameter of 200 nm compared to  $CoS_2/SKJ$  (Figure S4a,b). Besides, obvious agglomeration occurs in  $CoS_2$  plus SKJ, leading to a non-uniform distribution of  $CoS_2$  and KJ carbon.

The crystalline nature of the as-prepared materials is revealed by the X-ray diffraction (XRD) (Figure 2a). All the peaks can be unequivocally attributed to cubic  $CoS_2$  with the space group  $Pa\bar{3}$  (205) (JCPDS 41–1471),<sup>19</sup> confirming that the cobalt precursor was thermally sulfurized into cobalt sulfide. The crystal domain size of  $CoS_2$  along the (200)

direction is calculated to be 8.3 nm via the Scherrer equation, which coincides with the results observed in HRTEM. Moreover, the peak at  $23.8^\circ$  corresponds to a typical carbon (002) plane,<sup>23</sup> and its intensity in  $CoS_2/SKJ$  slightly decreased compared with that in KJ. This change reflects the weakened graphitic crystallinity, and correspondingly numerous defects along the (002) direction that were likely formed as a result of S doping in the carbon skeleton.<sup>24</sup> In addition to the XRD results, the existence of  $CoS_2$  is also confirmed by the characteristic peak at  $670\text{ cm}^{-1}$  in the Raman spectra for  $CoS_2/$



**Figure 4.** (a) ORR curves of various catalysts in  $O_2$ -saturated 0.1 M KOH solution at 1600 rpm. (b) LSV curves of  $CoS_2/SKJ$  at different rotating speeds (inset: K–L plots obtained under various potentials). (c) OER curves and (d) Tafel plots of various catalysts at 1600 rpm in  $N_2$ -saturated 0.1 M KOH electrolyte. (e) differences between the ORR  $E_{1/2}$  and OER  $E_{j=10}$  of different catalysts. (f) ORR and (g) OER activities of  $CoS_2/SKJ$  and  $CoS_2$  plus SKJ before and after 3500 cycles, respectively. (h) ORR and (i) OER chronoamperometric response of  $CoS_2/SKJ$  and Pt/C,  $CoS_2/SKJ$ , and Ir/C at a constant potential of 0.7 and 1.6 V, respectively.

SKJ (Figure 2b).<sup>25</sup> The Raman spectra of both KJ and  $CoS_2/SKJ$  show two scattering peaks located at around 1340 and 1590  $cm^{-1}$ , which can be assigned to the disorder-induced D band with a  $A_{2g}$  vibration mode of a defective  $C_6$  ring, and G band with a  $E_{2g}$  mode of  $sp^2$ -bonded C atoms, respectively.<sup>26,27</sup> The D/G intensity ratio ( $I_D/I_G$ ) of  $CoS_2/SKJ$  is higher than that of KJ, thus further revealing its higher defective nature and structural distortion arising from the S doping. Besides, an obvious red shift of the G band is found in  $CoS_2/SKJ$  (1586  $cm^{-1}$ ) compared with KJ carbon (1592  $cm^{-1}$ ), which is a typical characteristic of *n*-type substitutional doping. Such a phenomenon can be attributed to the elongation of C–C bonds induced by the S-doping, which weakens the bond strength and thus decreases the vibrational frequency.<sup>28,29</sup> The XRD results coupled with Raman spectroscopy confirms that S atoms have been successfully incorporated into the carbon framework with the formation of numerous defects within  $CoS_2/SKJ$ , and that the S doping of graphitized carbon can be achieved by our approach.

It is well-known that a high porosity and large surface area are crucial attributes of catalysts with good activity, and thus, the pore texture of the catalytic materials is investigated by  $N_2$  adsorption and desorption measurement. As displayed in Figure 2c, a typical type-IV isotherm with a characteristic H3

hysteresis loop in the medium pressure range reveals the mesoporous nature. The specific surface area of KJ is 1433  $m^2 g^{-1}$ , and its pore volume is 2.6  $cm^3 g^{-1}$ . Correspondingly, KJ exhibits a narrow pore size distribution (PSD) of around 4.0 nm (Figure 2d), which is slightly smaller than the size of  $CoS_2$  nanoparticles confined inside pores. This suitable pore size can effectively immobilize  $CoS_2$  nanoparticles and prohibit detachment from the carbon pores, thus presenting a “ship in a bottle” design. After the thermal sulfurization with the formation of  $CoS_2$  inside the pores, the specific surface area drops to 993  $m^2 g^{-1}$ , while the pore volume decreases to 2.0  $cm^3 g^{-1}$ . This high porosity of  $CoS_2/SKJ$  is favorable for exposing a high density of active sites and supplying large diffusion space for reactants, which are beneficial for its electrocatalytic performance. Compared to KJ,  $CoS_2/SKJ$  maintains similar shapes of the isotherm curve and PSD plots except with decreased pore volume, and there is no shift of the PSD peak position between  $CoS_2/SKJ$  and KJ. This strongly suggests that  $CoS_2$  nanoparticles were immobilized within the pores. The small  $CoS_2$  crystal size is derived from the adsorbed water vapor confined within the carbon pores, where its limited amount further determines the size of the cobalt-hydrolyzed product, followed by the sulfurization

process, in which CoS<sub>2</sub> is formed without particle agglomeration and crystal growth owing to the pore confinement effect.

The loading amount of CoS<sub>2</sub> within the carbon pores is evaluated by thermogravimetric analysis (TGA), as shown in Figure 3a. Commercially pure CoS<sub>2</sub> is also studied by TGA for determining the loaded CoS<sub>2</sub> content in CoS<sub>2</sub>/SKJ, which is calculated to be 15.5 wt %, while the carbon content is 84.5 wt % (see calculation details in the Supporting Information). The burned products of CoS<sub>2</sub>/SKJ collected after thermal treatment at 900 °C in air were investigated using XRD, as shown in Figure S5. To further investigate the elemental compositions and bonding configurations in CoS<sub>2</sub>/SKJ, X-ray photoelectron spectroscopy (XPS) is conducted (Figure 3b–d). The high-resolution C 1s spectrum (Figure 3b) not only shows peaks corresponding to C–C at 284.8 eV and C=O at 289.0 eV but also exhibits an apparent C–S peak located at 285.6 eV, implying that S was successfully doped into the carbon lattice network by forming the C–S covalent bond.<sup>30,31</sup> In the high-resolution Co 2p spectrum (Figure 3c), a pair of characteristic peaks located at 780.5 and 796.5 eV are assigned to Co 2p<sub>3/2</sub> and Co 2p<sub>1/2</sub> with two satellite peaks at 785.5 and 802.2 eV, respectively, confirming the presence of Co<sup>2+</sup> in the CoS<sub>2</sub> phase.<sup>32,33</sup> Figure S6 compares the Co 2p spectra of as-prepared CoS<sub>2</sub>/SKJ and pure CoS<sub>2</sub>. It is clearly seen that Co peaks in CoS<sub>2</sub>/SKJ slightly shift to the lower energy region compared to those of pure CoS<sub>2</sub>. This is because the electron cloud is expected to show a bias between CoS<sub>2</sub> and S-doping carbon framework, forming a strong electronic coupling between these two components. Figure 3d presents the S 2p spectrum, in which the peaks at 162.6 and 163.7 eV are attributed to S 2p<sub>3/2</sub> and S 2p<sub>1/2</sub>, respectively, corresponding to the disulfide S<sub>2</sub><sup>2-</sup>.<sup>34</sup> A pair of characteristic peaks appearing at 164.4 and 165.3 eV belong to C–S–C and C=S bonds, respectively, validating that our designed thermal sulfurization process leads to S incorporation into the carbon skeleton resulting in C–S bonded groups.<sup>32,35</sup> The existence of the C–S–C bond, which has been recognized as an effective active site, contributes to considerable catalytic activity.<sup>36</sup> The peak centered at 168.4 eV arises from a SO<sub>x</sub> species, such as sulfonate or sulfate, which is probably formed by the surface oxidation of sulfur due to the exposure in air.<sup>37,38</sup> Therefore, the S-doping and carbon defective nature of CoS<sub>2</sub>/SKJ have been unveiled by XRD, Raman, and XPS results, which plays a key role for enhancement of the electrocatalytic activity.

Hitherto, the above results and analysis have demonstrated that our designed small CoS<sub>2</sub> nanoparticles encapsulated inside pores of S-doped and highly defective carbon nanomaterials have been successfully prepared, thereby realizing a “ship in a bottle” design. All the exhibited features endow the product (CoS<sub>2</sub>/SKJ) with great potential as an exceptional electrocatalyst for Zn-air batteries.

The bifunctional electrocatalytic performance of CoS<sub>2</sub>/SKJ was evaluated via the linear sweep voltammetry (LSV) measurements. As a control, S-doped carbon was prepared by direct thermal sulfurization of KJ (denoted as SKJ). LSV measurements of CoS<sub>2</sub>+SKJ, SKJ, commercial CoS<sub>2</sub> nanoparticles and KJ, as well as noble-metal catalyst (*i.e.*, Pt/C and Ir/C) were conducted for comparison. The polarization curves of various prepared catalysts measured at a rotation speed of 1600 rpm are shown in Figure 4a. Compared to KJ, SKJ shows a higher onset potential of 0.80 V (*versus* the reversible hydrogen electrode, RHE) and diffusion-limited current density of 4.8 mA cm<sup>-2</sup>, which confirms the significant role

of S-doping in enhancing ORR catalytic activity. CoS<sub>2</sub> plus SKJ shows a low onset potential of 0.82 V and diffusion-limited current density of 4.8 mA cm<sup>-2</sup>, which is similar to the commercial CoS<sub>2</sub> nanoparticles (0.81 V and 4.1 mA cm<sup>-2</sup>). By comparison, CoS<sub>2</sub>/SKJ exhibits a prominent improvement on ORR performance, with a higher onset potential of 0.92 V and larger diffusion-limited current density of 5.2 mA cm<sup>-2</sup>. Moreover, CoS<sub>2</sub>/SKJ shows a half-wave potential ( $E_{1/2}$ ) of 0.84 V, which is only about 10 mV more negative than that of commercial Pt/C catalyst but much higher than that of CoS<sub>2</sub>+SKJ (0.76 V), SKJ (0.69 V), commercial CoS<sub>2</sub> nanoparticles (0.74 V), and KJ (0.66 V), highlighting the superior electrocatalytic activity of the CoS<sub>2</sub>/SKJ catalyst. To further investigate the electron-transfer kinetics of the CoS<sub>2</sub>/SKJ catalyst, polarization curves were measured at different rotation speeds. As shown in Figure 4b, CoS<sub>2</sub>/SKJ shows a well-defined plateau of diffusion-limited currents at all rotation speeds, where, as expected, the current densities increase with the rise of rotation speeds, which is owing to the expedited mass transfer of oxygen molecules from the electrolyte to the electrode surface. More importantly, the Koutecky–Levich (K–L) plots of CoS<sub>2</sub>/SKJ present good linearity and near parallelism at different potentials, revealing the first-order reaction kinetics toward the concentration of dissolved oxygen.<sup>39</sup> The electron-transfer number ( $n$ ) for CoS<sub>2</sub>/SKJ obtained from the K–L plot slope is 4.0, signifying the fast kinetics with a four-electron-transfer reaction pathway to reduce oxygen directly to OH<sup>-</sup>. The superior reaction kinetics are attributed to the fast electron transfer benefiting from an interconnected conductive carbon framework, which not only surrounds the CoS<sub>2</sub>-impregnated pores but also is present within the whole composite. These results confirm the superior ORR catalytic activity of CoS<sub>2</sub>/SKJ.

Oxygen evolution activities are also investigated to confirm the suitability of CoS<sub>2</sub>/SKJ as bifunctional electrocatalysts for both ORR and OER. Figure 4c illustrates the LSV behavior of the as-prepared catalysts in N<sub>2</sub>-saturated 0.1 M KOH. As expected, CoS<sub>2</sub>/SKJ exhibits a OER potential of only 1.58 V at the current density of 10 mA cm<sup>-2</sup>, which is smaller than CoS<sub>2</sub> plus SKJ (1.66 V), SKJ (1.73 V), commercial CoS<sub>2</sub> (1.65 V), and KJ (1.76 mV), demonstrating the smallest over-potential of CoS<sub>2</sub>/SKJ among the obtained catalysts. In particular, the over-potential at 10 mA cm<sup>-2</sup> ( $\eta_{j=10}$ ) of CoS<sub>2</sub>/SKJ (350 mV) is even smaller than that of commercial Ir/C catalyst (380 mV), revealing its excellent OER electrocatalytic activity. The fast OER kinetics of CoS<sub>2</sub>/SKJ is further revealed by its smaller Tafel slope (83 mV dec<sup>-1</sup>) relative to the other catalysts (Figure 4d). In addition, the activity improvement from KJ to SKJ reflects that S doping effectively contributes to OER catalytic activity enhancement.

To reveal the bifunctional activity of the CoS<sub>2</sub>/SKJ catalyst, the potential difference  $\Delta E$  between the ORR half-wave potential ( $E_{1/2}$ ) and OER potential at 10 mA cm<sup>-2</sup> ( $E_{j=10}$ ) is assessed (Figure S7), with a smallest value of  $\Delta E$  ( $\Delta E = E_{j=10} - E_{1/2}$ ) indicating superior catalytic bifunctionality. The over-potential toward ORR and OER is reflected by comparing with the  $E^{\circ}$  (OH<sup>-</sup>/O<sub>2</sub>) = 1.23 V. As illustrated in Figure 4e and Table S1, CoS<sub>2</sub>/SKJ exhibits a desirable  $\Delta E$  of 0.74 V, smaller than Pt/C coupled with Ir/C, as well as the other as-prepared catalysts. More importantly, the low  $\Delta E$  of CoS<sub>2</sub>/SKJ outperforms the majority of well-developed bifunctional catalysts reported recently (Table S2), unveiling the superior bifunctional electrocatalytic nature of CoS<sub>2</sub>/SKJ.



a certain current density, the battery energy efficiency is based on the ratio of the discharge potential to the charge potential.<sup>40</sup> As shown in Figure 5c, at the current density of 120 mA cm<sup>-2</sup>, the energy efficiency of CoS<sub>2</sub>/SKJ is 1.5 times higher than that of the noble-metal benchmark, which is attributed to its provision of unimpeded access for reactants reaching toward the active sites (*i.e.*, the high-efficiency catalyst utilization). Moreover, the more salient electrochemical performance of the CoS<sub>2</sub>/SKJ air electrode is also due to the interconnected conductive carbon network and interpenetrating porous structure, which guarantee fast charge transfer, as well as enhanced accessibility of oxygen species and electrolyte to the electrocatalytic sites.

To further investigate the efficiency and cycle stability of CoS<sub>2</sub>/SKJ for the Zn-air battery, a galvanostatic charge–discharge test is performed at a high current density of 25 mA cm<sup>-2</sup>, which cycles with 40 min charging and 40 min discharging. As illustrated in Figure 5d, the initial charge–discharge voltage gap of CoS<sub>2</sub>/SKJ is 0.92 V, smaller than that of the noble-metal benchmark Pt/C plus Ir/C catalyst (1.01 V). More importantly, the Zn–air battery assembled with CoS<sub>2</sub>/SKJ exhibits a superior durability without noticeable voltage fading for both charge and discharge processes over 340 h of continuous operation, whereas the battery using Pt/C plus Ir/C catalyst delivers a limited cyclability with operation time of less than 30 h. The poor stability of Pt/C plus Ir/C catalyst is because of the dissolution and redeposition, migration and aggregation, and sintering of the noble-metal particles as well as the formation of the insulating platinum oxides under operational conditions.<sup>50</sup> These could lead to an increase in the particles' size and the particle detachment, causing the irreversible loss of active sites and degradation of electrocatalytic performance.<sup>51</sup> The battery energy efficiency of Pt/C–Ir/C hybrid catalyst reduces far faster than that of CoS<sub>2</sub>/SKJ, leading to significant charge and discharge performance losses. Particularly, the battery with CoS<sub>2</sub>/SKJ can also withstand a very high current density (25 mA cm<sup>-2</sup>), presenting an extremely low decaying rate of 0.039 millivolts per cycle and a small voltage gap of 0.93 V after 255 cycles, much better than the noble-metal benchmark with a high voltage decaying rate (32.44 millivolts per cycle) and voltage gap (1.74 V) (Figure 5e). Such long-lasting cyclability over this time scale in this work is evidently superior to other recently reported results, as shown in Figure 5f and associated detailed information in Table S4. Undoubtedly, the impressive stability and long-term rechargeability of CoS<sub>2</sub>/SKJ can be attributed to the pore confinement design. Specifically, the carbon pores provide spatial confinement to restrict the overgrowth of active CoS<sub>2</sub> nanoparticles and prevent them from aggregating during the catalysis and cycle process. At the same time, S doping within the carbon framework can modify the electronic and steric pore environment with the formation of the C–S bond, which may afford strong affinity toward CoS<sub>2</sub>, which can, in turn, immobilize CoS<sub>2</sub> nanoparticles inside the pores. To affirm the structural evolution upon cycling as the evidence for the above analysis, SEM, TEM, and STEM observations were carried out on the CoS<sub>2</sub>/SKJ electrode after cycling over 340 h. Figure S9 demonstrates that the intact 3D architecture was retained during the battery cycling. CoS<sub>2</sub> nanoparticles are found still immobilized well inside the carbon pores with an original size of around 8.0 nm without obvious agglomeration or detachment (Figure 5g and h). This manifests the robust carbon framework structure and effective pore spatial confine-

ment effect, which contributes to the excellent durability. Finally, the application prospect of the device is demonstrated in Figure Si. A total of three CoS<sub>2</sub>/SKJ-batteries power a mini-fan equipped with light-emitting diode (LED), which operates at a minimum voltage of 3.6 V.

All of the above results highlight the excellent bifunctional electrocatalytic activity and long-term durability of CoS<sub>2</sub>/SKJ, which profit from the following aspects. First, the pore spatial confinement effect makes fine active CoS<sub>2</sub> nanoparticles root inside graphitized carbon pores, which not only presents a high surface-to-volume ratio to facilitate the exposure of more catalytically active sites but also effectively inhibits overgrowth and agglomeration of nanocatalysts during a long-cycling catalytic process. Second, the formation of the C–S–C bond derived from S doping into the carbon skeleton acts as an important catalytically active site for promoting ORR and OER.<sup>36</sup> As per previous reports,<sup>52</sup> it can break the electro-neutrality of carbon to create positively charged sites favorable for O<sub>2</sub> adsorption, and this parallel diatomic adsorption can effectively weaken the O–O bonding to further promote the direct reduction of oxygen to OH<sup>-</sup> via a four-electron process. Additionally, the S doping within the carbon framework can also enhance the spin density, which plays a pivotal role in determining the catalytically active sites.<sup>53</sup> Third, the defect-rich interfaces function as atomic traps, which can effectively boost the localization of oxygen species toward active sites, promoting the catalytic activity and stability. Moreover, the graphitized carbon framework not only intimately enfolds the CoS<sub>2</sub> nanoparticles but also interpenetrates over the whole composite, building up an interconnected conductive network to offer fast electron transfer. More importantly, the interpenetrating porous structures erect a robust 3D architecture as the nanoreactors for ion and oxygen species transfer inside and through the CoS<sub>2</sub>/SKJ catalyst, which significantly improves the kinetics for electrocatalytic processes. This architecture capitalizes on the synergistic interactions between CoS<sub>2</sub> nanoparticles, carbon defects, and intimate covalent bonds (*i.e.*, C–S bonding) from S doping under the steric pore environment, which endow CoS<sub>2</sub>/SKJ with prominent catalytic performance.

## CONCLUSIONS

In this work, an exquisite bifunctional catalyst consisting of fine CoS<sub>2</sub> nanoparticles encapsulated inside the defective carbon pores is designed and successfully accomplished via precursor impregnation, hydrolysis and subsequent thermal sulfurization. This methodology realizes the combination of excellent catalytic kinetics and electrical conductivity provided by the interconnecting porous carbon framework acting as a nano-reactor, which effectively restricts the nucleation (*i.e.*, overgrowth) and agglomeration of nanoparticles during catalysis. Therefore, this exquisitely designed catalyst, harvesting the synergistic effect between defect-rich interfaces (*i.e.*, S-doped pores) and effective catalytic active sites (CoS<sub>2</sub> and C–S–C bonding) guarantees superior electrochemical performance. The as-developed CoS<sub>2</sub>/SKJ catalyst exhibits excellent catalytic activity and durability for both ORR and OER with a  $\Delta E$  of 0.74 V, unveiling its excellent bifunctional catalytic ability for rechargeable Zn–air batteries. Encouragingly, when integrated within an air electrode, CoS<sub>2</sub>/SKJ exhibits low charge and discharge over-potential (*i.e.*, high energy efficiency), large peak power density, and exceptionally stable cyclability of over 340 h at a very high current density of 25 mA cm<sup>-2</sup>, out-

performing noble-metal benchmarks and other recently reported results. This work provides a guide to designing efficient and durable non-precious-metal bifunctional electrocatalysts for metal–air batteries, and we believe that such a universal “ship in a bottle” design of impregnating fine metal nanoparticles inside pores will deliver an instructive model of material engineering for implementation in various fields.

## METHODS

**Preparation of CoS<sub>2</sub>/SKJ.** Ketjen Black EC600JD (KJ) was purchased from MTI Corporation, China. The other chemicals were purchased from Sigma-Aldrich and of analytical grade without further purification. In a typical synthesis, 80 mg KJ carbon with adsorbed water vapor was placed inside a fused quartz tube under ammonium gas flow for several minutes at room temperature. Subsequently, the sample was immersed into saturated cobalt(II) acetylacetonate/ethyl acetate solution for 10 h. Then, the solid sample was filtrated and washed with ethyl acetate several times. After drying at 80 °C for 8 h, the collected sample was transferred to the center of a tube furnace. An alumina boat containing 2 g of sulfur powder was placed at the farthest upstream position in the tube furnace. The tube was purged of air with a steady flow of argon gas at 30 sccm, and the sulfurization process was performed at 400 °C for 2 h, resulting in the formation of the CoS<sub>2</sub>/SKJ sample.

**Preparation of CoS<sub>2</sub> Plus SKJ.** KJ was first mechanically mixed with commercial CoS<sub>2</sub> nanoparticles with the same CoS<sub>2</sub> content as CoS<sub>2</sub>/SKJ. Then, the as-prepared sample underwent the above sulfurization process to obtain CoS<sub>2</sub> plus SKJ.

**Preparation of SKJ.** KJ carbon was directly subjected to the above sulfurization process to produce SKJ.

**Materials Characterizations.** Microscopic morphology, EDS, and EELS data of materials were collected by SEM using an FEI Quanta FEG 250 ESEM microscope and TEM using a JEOL 2010F TEM/STEM equipped with a large solid angle for high X-ray throughput, scanning, scanning and transmission, and a Gatan imaging filter for energy filtered imaging. XRD was carried out using a Rigaku MiniFlex 600 X-ray diffractometer equipped with a Cu K $\alpha$  irradiation. To collect Raman spectra, a 532 nm laser source was employed. The Thermal Scientific K- $\alpha$  spectrometer was used to collect XPS spectra. TGA was performed on a TA Instruments Q500 under air atmosphere. Nitrogen adsorption–desorption isotherms were measured at liquid nitrogen temperature (–196 °C) by using the Micromeritics ASAP 2020 analyzer; the Brunauer–Emmett–Teller equation was used to calculate the specific surface area, and the Barrett–Joyner–Halenda model was used to determine the pore size distribution.

**Electrochemical Measurements.** The electrocatalytic performance was investigated using an electrochemical workstation (Biologic VSP 300) with a three-electrode configuration and rotating disk electrode (RDE). A glassy carbon electrode (GC; 0.196 cm<sup>2</sup>) and a graphite rod were used as the working and counter electrodes, respectively. All of the results were obtained with reference to a saturated calomel electrode (SCE) followed by the calibration to the RHE based on the Nernst equation:  $E_{\text{RHE}} = E_{\text{SCE}} + 0.059 \times \text{pH} + 0.241$ . The homogeneous catalyst ink was prepared by dispersing 2 mg of catalyst into 500  $\mu\text{L}$  of 0.3 wt % Nafion ethanol solution under ultrasonication for 30 min. Then, a loading of 0.26 mg cm<sup>–2</sup> was achieved by pipetting 13  $\mu\text{L}$  of ink on GC surface. The commercial Pt/C and Ir/C catalysts were also prepared via the same procedure as respective ORR and OER benchmarks. The calculation of the electron-transfer number per oxygen molecule is based on the K–L equation:  $\frac{1}{j} = \frac{1}{j_k} + \frac{1}{B\omega^{1/2}}$ , where  $j_k$  is the kinetic current and  $B$  is Levich slope:  $B = 0.2nFD_0^{2/3}C_0\nu^{-1/6}$  ( $n$  is the number of transferred electrons,  $F$  is the Faraday constant,  $D_0$  is the oxygen diffusion coefficient of  $1.9 \times 10^{-5}$  cm<sup>2</sup> s<sup>–1</sup>,  $C_0$  is the oxygen saturated concentration of  $1.1 \times 10^{-6}$  mol cm<sup>–3</sup>, and  $\nu$  is the kinematic viscosity of 0.01 cm<sup>2</sup> s<sup>–1</sup>).

**Assembly of Zn–Air Batteries.** The prototypes applied an open-cell configuration, which contain catalyst-sprayed gas diffusion layer (GDL, SGL Carbon 39 BC, Ion Power Inc.) with a catalyst loading of 1.0 mg cm<sup>–2</sup> acting as the air electrode and a polished high-purity (99.99%) zinc plate acting as the anode. The potassium hydroxide solution plus zinc acetate solution was filled into the prototypes as electrolyte and supplemented regularly. For comparison, the mixture of commercial Pt/C and Ir/C catalysts (1:1 mass ratio) was also sprayed on GDL with the same fabrication process as the performance benchmark. The battery testing was performed on a Land tester (Land Electronic Co., Ltd., Wuhan) under ambient atmosphere.

## ASSOCIATED CONTENT

### Supporting Information

The Supporting Information is available free of charge on the ACS Publications website at DOI: 10.1021/acsnano.9b02315.

Calculation of the loading content of CoS<sub>2</sub> in CoS<sub>2</sub>/SKJ composite, the morphology and structure of experimental materials, the size distribution of CoS<sub>2</sub> nanoparticles within carbon pores, XRD patterns for burning products of CoS<sub>2</sub>/SKJ in air; entire LSV curves for bifunctional electrocatalytic activities, and a comparison of bifunctional electrocatalytic activities of catalysts and cyclability of Zn–air batteries between this work and recently reported results (PDF)

## AUTHOR INFORMATION

### Corresponding Author

\*E-mail: zhwchen@uwaterloo.ca.

### ORCID

Dan Luo: 0000-0001-9289-888X

Zachary Paul Cano: 0000-0002-2433-297X

Zhongwei Chen: 0000-0003-3463-5509

### Notes

The authors declare no competing financial interest.

## ACKNOWLEDGMENTS

The authors greatly appreciate the support from by the Natural Sciences and Engineering Research Council of Canada (NSERC), University of Waterloo, Waterloo Institute for Nanotechnology, and the Canadian Centre for Electron Microscopy at McMaster University.

## REFERENCES

- (1) Katsounaros, I.; Cherevko, S.; Zeradjanin, A. R.; Mayrhofer, K. J. Oxygen Electrochemistry as a Cornerstone for Sustainable Energy Conversion. *Angew. Chem., Int. Ed.* **2014**, *53*, 102–121.
- (2) Balogun, M.-S.; Yang, H.; Luo, Y.; Qiu, W.; Huang, Y.; Liu, Z.-Q.; Tong, Y. Achieving High Gravimetric Energy Density for Flexible Lithium-Ion Batteries Facilitated by Core-Double-Shell Electrodes. *Energy Environ. Sci.* **2018**, *11*, 1859–1869.
- (3) Lee, J.-S.; Tai Kim, S.; Cao, R.; Choi, N.-S.; Liu, M.; Lee, K. T.; Cho, J. Metal-Air Batteries with High Energy Density: Li-Air versus Zn-Air. *Adv. Energy Mater.* **2011**, *1*, 34–50.
- (4) Li, Y.; Dai, H. Recent Advances in Zinc–Air Batteries. *Chem. Soc. Rev.* **2014**, *43*, 5257–5275.
- (5) Li, Y.; Lu, J. Metal–Air Batteries: Will They Be the Future Electrochemical Energy Storage Device of Choice? *ACS Energy Lett.* **2017**, *2*, 1370–1377.
- (6) Cao, R.; Lee, J.-S.; Liu, M.; Cho, J. Recent Progress in Non-Precious Catalysts for Metal-Air Batteries. *Adv. Energy Mater.* **2012**, *2*, 816–829.
- (7) Lee, J.-S.; Lee, T.; Song, H.-K.; Cho, J.; Kim, B.-S. Ionic Liquid Modified Graphene Nanosheets Anchoring Manganese Oxide Nano-

particles as Efficient Electrocatalysts for Zn–Air Batteries. *Energy Environ. Sci.* **2011**, *4*, 4148–4154.

(8) Lee, D. U.; Xu, P.; Cano, Z. P.; Kashkooli, A. G.; Park, M. G.; Chen, Z. Recent Progress and Perspectives on Bi-Functional Oxygen Electrocatalysts for Advanced Rechargeable Metal–Air Batteries. *J. Mater. Chem. A* **2016**, *4*, 7107–7134.

(9) Yin, J.; Li, Y.; Lv, F.; Fan, Q.; Zhao, Y.-Q.; Zhang, Q.; Wang, W.; Cheng, F.; Xi, P.; Guo, S. NiO/CoN Porous Nanowires as Efficient Bifunctional Catalysts for Zn–Air Batteries. *ACS Nano* **2017**, *11*, 2275–2283.

(10) Liu, Z.-Q.; Cheng, H.; Li, N.; Ma, T. Y.; Su, Y.-Z. ZnCo<sub>2</sub>O<sub>4</sub> Quantum Dots Anchored on Nitrogen-Doped Carbon Nanotubes as Reversible Oxygen Reduction/Evolution Electrocatalysts. *Adv. Mater.* **2016**, *28*, 3777–3784.

(11) Cheng, H.; Li, M.-L.; Su, C.-Y.; Li, N.; Liu, Z.-Q. Cu–Co Bimetallic Oxide Quantum Dot Decorated Nitrogen-Doped Carbon Nanotubes: A High-Efficiency Bifunctional Oxygen Electrode for Zn–Air Batteries. *Adv. Funct. Mater.* **2017**, *27*, 1701833.

(12) Cheng, H.; Chen, J.-M.; Li, Q.-J.; Su, C.-Y.; Chen, A.-N.; Zhang, J.-X.; Liu, Z.-Q.; Tong, Y. A Modified Molecular Framework Derived Highly Efficient Mn–Co–Carbon Cathode for a Flexible Zn–Air Battery. *Chem. Commun.* **2017**, *53*, 11596–11599.

(13) Xia, B. Y.; Yan, Y.; Li, N.; Wu, H. B.; Lou, X. W.; Wang, X. A Metal–Organic Framework-Derived Bifunctional Oxygen Electrocatalyst. *Nat. Energy* **2016**, *1*, 15006.

(14) Liu, X.; Park, M.; Kim, M. G.; Gupta, S.; Wu, G.; Cho, J. Integrating NiCo Alloys with Their Oxides as Efficient Bifunctional Cathode Catalysts for Rechargeable Zinc–Air Batteries. *Angew. Chem., Int. Ed.* **2015**, *54*, 9654–9658.

(15) Wu, X.; Han, X.; Ma, X.; Zhang, W.; Deng, Y.; Zhong, C.; Hu, W. Morphology-Controllable Synthesis of Zn–Co-Mixed Sulfide Nanostructures on Carbon Fiber Paper Toward Efficient Rechargeable Zinc–Air Batteries and Water Electrolysis. *ACS Appl. Mater. Interfaces* **2017**, *9*, 12574–12583.

(16) Higgins, D.; Hoque, M. A.; Seo, M. H.; Wang, R.; Hassan, F.; Choi, J.-Y.; Pritzker, M.; Yu, A.; Zhang, J.; Chen, Z. Development and Simulation of Sulfur-Doped Graphene Supported Platinum with Exemplary Stability and Activity Towards Oxygen Reduction. *Adv. Funct. Mater.* **2014**, *24*, 4325–4336.

(17) Yan, D.; Li, Y.; Huo, J.; Chen, R.; Dai, L.; Wang, S. Defect Chemistry of Nonprecious-Metal Electrocatalysts for Oxygen Reactions. *Adv. Mater.* **2017**, *29*, 1606459.

(18) Liu, Z.; Zhao, Z.; Wang, Y.; Dou, S.; Yan, D.; Liu, D.; Xia, Z.; Wang, S. *In Situ* Exfoliated, Edge-Rich, Oxygen-Functionalized Graphene from Carbon Fibers for Oxygen Electrocatalysis. *Adv. Mater.* **2017**, *29*, 1606207.

(19) Faber, M. S.; Dziejcz, R.; Lukowski, M. A.; Kaiser, N. S.; Ding, Q.; Jin, S. High-Performance Electrocatalysis Using Metallic Cobalt Pyrite (CoS<sub>2</sub>) Micro- and Nanostructures. *J. Am. Chem. Soc.* **2014**, *136*, 10053–10061.

(20) Kiciński, W.; Szala, M.; Bystrzejewski, M. Sulfur-Doped Porous Carbons: Synthesis and Applications. *Carbon* **2014**, *68*, 1–32.

(21) Shadik, Z.; Cao, M.-H.; Ding, F.; Sang, L.; Fu, Z.-W. Improved Electrochemical Performance of CoS<sub>2</sub>–MWCNT Nanocomposites for Sodium-Ion Batteries. *Chem. Commun.* **2015**, *51*, 10486–10489.

(22) Huang, Z. X.; Wang, Y.; Wong, J. I.; Shi, W. H.; Yang, H. Y. Synthesis of Self-Assembled Cobalt Sulphide Coated Carbon Nanotube and Its Superior Electrochemical Performance as Anodes for Li-Ion Batteries. *Electrochim. Acta* **2015**, *167*, 388–395.

(23) Kuang, M.; Wang, Q.; Han, P.; Zheng, G. Cu, Co-Embedded N-Enriched Mesoporous Carbon for Efficient Oxygen Reduction and Hydrogen Evolution Reactions. *Adv. Energy Mater.* **2017**, *7*, 1700193.

(24) Xing, Z.; Gao, N.; Qi, Y.; Ji, X.; Liu, H. Influence of Enhanced Carbon Crystallinity of Nanoporous Graphite on the Cathode Performance of Microbial Fuel Cells. *Carbon* **2017**, *115*, 271–278.

(25) Tang, J.; Shen, J.; Li, N.; Ye, M. A Free Template Strategy for the Synthesis of CoS<sub>2</sub>-Reduced Graphene Oxide Nanocomposite with Enhanced Electrode Performance for Supercapacitors. *Ceram. Int.* **2014**, *40*, 15411–15419.

(26) Zhang, Z.; Luo, D.; Lui, G.; Li, G.; Jiang, G.; Cano, Z. P.; Deng, Y.-P.; Du, X.; Yin, S.; Chen, Y.; Zhang, M.; Yan, Z.; Chen, Z. *In-Situ* Ion-Activated Carbon Nanospheres with Tunable Ultramicroporosity for Superior CO<sub>2</sub> Capture. *Carbon* **2019**, *143*, S31–S41.

(27) Mera, G.; Navrotsky, A.; Sen, S.; Kleebe, H.-J.; Riedel, R. Polymer-Derived SiCN and SiOC Ceramics—Structure and Energetics at the Nanoscale. *J. Mater. Chem. A* **2013**, *1*, 3826–3836.

(28) Shahzad, F.; Kumar, P.; Yu, S.; Lee, S.; Kim, Y.-H.; Hong, S. M.; Koo, C. M. Sulfur-Doped Graphene Laminates for EMI Shielding Applications. *J. Mater. Chem. C* **2015**, *3*, 9802–9810.

(29) Huang, H.; Zhu, J.; Zhang, W.; Tiwary, C. S.; Zhang, J.; Zhang, X.; Jiang, Q.; He, H.; Wu, Y.; Huang, W.; Ajayan, P. M.; Yan, Q. Controllable Codoping of Nitrogen and Sulfur in Graphene for Highly Efficient Li-Oxygen Batteries and Direct Methanol Fuel Cells. *Chem. Mater.* **2016**, *28*, 1737–1745.

(30) Xu, Q.; Pu, P.; Zhao, J.; Dong, C.; Gao, C.; Chen, Y.; Chen, J.; Liu, Y.; Zhou, H. Preparation of Highly Photoluminescent Sulfur-Doped Carbon Dots for Fe (III) Detection. *J. Mater. Chem. A* **2015**, *3*, 542–546.

(31) Liu, Z.; Zhang, Z.; Jia, Z.; Zhao, L.; Zhang, T.; Xing, W.; Komarneni, S.; Subhan, F.; Yan, Z. New Strategy to Prepare Ultramicroporous Carbon by Ionic Activation for Superior CO<sub>2</sub> Capture. *Chem. Eng. J.* **2018**, *337*, 290–299.

(32) Niu, W.; Li, Z.; Marcus, K.; Zhou, L.; Li, Y.; Ye, R.; Liang, K.; Yang, Y. Surface-Modified Porous Carbon Nitride Composites as Highly Efficient Electrocatalyst for Zn–Air Batteries. *Adv. Energy Mater.* **2018**, *8*, 1701642.

(33) Cui, X.; Xie, Z.; Wang, Y. Novel CoS<sub>2</sub> Embedded Carbon Nanocages by Direct Sulfurizing Metal–Organic Frameworks for Dye-Sensitized Solar Cells. *Nanoscale* **2016**, *8*, 11984–11992.

(34) Samad, L.; Cabán-Acevedo, M.; Shearer, M. J.; Park, K.; Hamers, R. J.; Jin, S. Direct Chemical Vapor Deposition Synthesis of Phase-Pure Iron Pyrite (FeS<sub>2</sub>) Thin Films. *Chem. Mater.* **2015**, *27*, 3108–3114.

(35) Li, M.; Liu, C.; Zhao, H.; An, H.; Cao, H.; Zhang, Y.; Fan, Z. Tuning Sulfur Doping in Graphene for Highly Sensitive Dopamine Biosensors. *Carbon* **2015**, *86*, 197–206.

(36) El-Sawy, A. M.; Mosa, I. M.; Su, D.; Guild, C. J.; Khalid, S.; Joesten, R.; Rusling, J. F.; Suib, S. L. Controlling the Active Sites of Sulfur-Doped Carbon Nanotube-Graphene Nanolobes for Highly Efficient Oxygen Evolution and Reduction Catalysis. *Adv. Energy Mater.* **2016**, *6*, 1501966.

(37) Ye, J.; He, F.; Nie, J.; Cao, Y.; Yang, H.; Ai, X. Sulfur/Carbon Nanocomposite-Filled Polyacrylonitrile Nanofibers as a Long Life and High Capacity Cathode for Lithium–Sulfur Batteries. *J. Mater. Chem. A* **2015**, *3*, 7406–7412.

(38) Sun, D.; Ban, R.; Zhang, P.-H.; Wu, G.-H.; Zhang, J.-R.; Zhu, J.-J. Hair Fiber as a Precursor for Synthesizing of Sulfur- and Nitrogen-Co-Doped Carbon Dots with Tunable Luminescence Properties. *Carbon* **2013**, *64*, 424–434.

(39) Li, G.; Wang, X.; Fu, J.; Li, J.; Park, M. G.; Zhang, Y.; Lui, G.; Chen, Z. Pomegranate-Inspired Design of Highly Active and Durable Bifunctional Electrocatalysts for Rechargeable Metal–Air Batteries. *Angew. Chem., Int. Ed.* **2016**, *55*, 4977–4982.

(40) Fu, J.; Cano, Z. P.; Park, M. G.; Yu, A.; Fowler, M.; Chen, Z. Electrically Rechargeable Zinc–Air Batteries: Progress, Challenges, and Perspectives. *Adv. Mater.* **2017**, *29*, 1604685.

(41) Li, C.; Han, X.; Cheng, F.; Hu, Y.; Chen, C.; Chen, J. Phase and Composition Controllable Synthesis of Cobalt Manganese Spinel Nanoparticles towards Efficient Oxygen Electrocatalysis. *Nat. Commun.* **2015**, *6*, 7345.

(42) Park, J.; Risch, M.; Nam, G.; Park, M.; Shin, T. J.; Park, S.; Kim, M. G.; Shao-Horn, Y.; Cho, J. Single Crystalline Pyrochlore Nanoparticles with Metallic Conduction as Efficient Bi-Functional Oxygen Electrocatalysts for Zn–Air Batteries. *Energy Environ. Sci.* **2017**, *10*, 129–136.

(43) Deng, Y.-P.; Jiang, Y.; Luo, D.; Fu, J.; Liang, R.; Cheng, S.; Bai, Z.; Liu, Y.; Lei, W.; Yang, L.; Zhu, J.; Chen, Z. Hierarchical Porous Double-Shelled Electrocatalyst with Tailored Lattice Alkalinity toward

Bifunctional Oxygen Reactions for Metal–Air Batteries. *ACS Energy Lett.* **2017**, *2*, 2706–2712.

(44) Liu, G.; Li, J.; Fu, J.; Jiang, G.; Lui, G.; Luo, D.; Deng, Y.; Zhang, J.; Cano, Z. P.; Yu, A.; Su, D.; Bai, Z.; Yang, L.; Chen, Z. An Oxygen-Vacancy-Rich Semiconductor-Supported Bifunctional Catalyst for Efficient and Stable Zinc–Air Batteries. *Adv. Mater.* **2018**, *1806761*.

(45) Yang, H. B.; Miao, J.; Hung, S.-F.; Chen, J.; Tao, H. B.; Wang, X.; Zhang, L.; Chen, R.; Gao, J.; Chen, H. M.; Dai, L.; Liu, B. Identification of Catalytic Sites for Oxygen Reduction and Oxygen Evolution in N-Doped Graphene Materials: Development of Highly Efficient Metal-Free Bifunctional Electrocatalyst. *Sci. Adv.* **2016**, *2*, No. e1501122.

(46) Wang, T.; Kou, Z.; Mu, S.; Liu, J.; He, D.; Amiin, I. S.; Meng, W.; Zhou, K.; Luo, Z.; Chaemchuen, S.; Verpoort, F. 2D Dual-Metal Zeolitic-Imidazolate-Framework-(ZIF)-Derived Bifunctional Air Electrodes with Ultrahigh Electrochemical Properties for Rechargeable Zinc-Air Batteries. *Adv. Funct. Mater.* **2018**, *28*, 1705048.

(47) Zhang, M.; Dai, Q.; Zheng, H.; Chen, M.; Dai, L. Novel MOF-Derived Co@N-C Bifunctional Catalysts for Highly Efficient Zn-Air Batteries and Water Splitting. *Adv. Mater.* **2018**, *30*, 1705431.

(48) Lee, D. U.; Park, M. G.; Park, H. W.; Seo, M. H.; Wang, X.; Chen, Z. Highly Active and Durable Nanocrystal-Decorated Bifunctional Electrocatalyst for Rechargeable Zinc-Air Batteries. *ChemSusChem* **2015**, *8*, 3129–3138.

(49) Wang, Z.; Li, B.; Ge, X.; Goh, F. W. T.; Zhang, X.; Du, G.; Wu, D.; Liu, Z.; Hor, T. S. A.; Zhang, H.; Zong, Y. Co@Co<sub>3</sub>O<sub>4</sub>@PPD Core@birefractive Nanoparticle-Based Composite as an Efficient Electrocatalyst for Oxygen Reduction Reaction. *Small* **2016**, *12*, 2580–2587.

(50) Chen, Z.; Waje, M.; Li, W.; Yan, Y. Supportless Pt and PtPd Nanotubes as Electrocatalysts for Oxygen-Reduction Reactions. *Angew. Chem., Int. Ed.* **2007**, *46*, 4060–4063.

(51) Zadick, A.; Dubau, L.; Sergent, N.; Berthomé, G.; Chatenet, M. Huge Instability of Pt/C Catalysts in Alkaline Medium. *ACS Catal.* **2015**, *5*, 4819–4824.

(52) Yang, Z.; Yao, Z.; Li, G.; Fang, G.; Nie, H.; Liu, Z.; Zhou, X.; Chen, X.; Huang, S. Sulfur-Doped Graphene as an Efficient Metal-Free Cathode Catalyst for Oxygen Reduction. *ACS Nano* **2012**, *6*, 205–211.

(53) Zhang, L.; Xia, Z. Mechanisms of Oxygen Reduction Reaction on Nitrogen-Doped Graphene for Fuel Cells. *J. Phys. Chem. C* **2011**, *115*, 11170–11176.